

## RESEARCH ARTICLE

# Impact of assimilating Aeolus observations in the global model ICON: A global statistical overview

Anne Martin<sup>1</sup>  | Martin Weissmann<sup>2</sup> | Alexander Cress<sup>3</sup>

<sup>1</sup>Ludwig-Maximilians-Universität,  
Meteorologisches Institut, Munich,  
Germany

<sup>2</sup>Institut für Meteorologie und Geophysik,  
Universität Wien, Vienna, Austria

<sup>3</sup>Deutscher Wetterdienst (DWD),  
Offenbach am Main, Offenbach, Germany

**Correspondence**

Anne Martin,  
Ludwig-Maximilians-Universität,  
Meteorologisches Institut,  
Theresienstraße 37, 80333 München,  
Germany.

Email:

[anne.martin@physik.uni-muenchen.de](mailto:anne.martin@physik.uni-muenchen.de)**Funding information**

Bundesministerium für Wirtschaft und  
Energie, Grant/Award Number:  
50EE1721A

**Abstract**

Global wind profiles provided by the satellite mission Aeolus are an important recent supplement to the Global Observing System. This study investigates the impact of Aeolus horizontal line-of-sight wind observations in the operational global assimilation and forecasting system of Deutscher Wetterdienst that is based on the Icosahedral Nonhydrostatic (ICON) model. For this purpose, an observing system experiment was conducted and evaluated for a 3-month period from July 2020 to October 2020. The Aeolus Rayleigh clear and Mie cloudy data quality and consistency were derived from observation minus background statistics. To correct for an altitude-dependent bias, a model-based bias correction scheme has been implemented. Comparisons of the systematic changes in the analysis and the respective forecasts provide an overview of the overall impact of the Aeolus horizontal line-of-sight wind assimilation in ICON. Increased influence of Aeolus wind profiles is found in jet regimes (e.g., amplification of the zonal wind component), around large-scale circulation systems, and convectively active areas in the Tropics. The reduction in forecast error is largest in the tropical upper troposphere and stratosphere, as well as in the mid and upper troposphere of the Southern Hemisphere. The Northern Hemisphere shows a somewhat smaller but still beneficial impact of Aeolus observations. The verification with other conventional observations shows a mean relative reduction in short-range forecast error between 0.1% and 0.6% in the Northern Hemisphere and up to 1.6% in the Tropics and the Southern Hemisphere. When verifying against the European Centre for Medium-Range Weather Forecast Reanalysis v5, forecast errors of zonal wind, temperature, and geopotential up to 5 days lead time are reduced by 2–4% on global average and up to 5–8% around the tropical tropopause.

**KEYWORDS**

Aeolus mission, data assimilation, Doppler wind lidar, NWP, observation impact, observing system experiment

## 1 | INTRODUCTION

Knowledge of the three-dimensional (3D) global wind field is fundamental for describing the physical state of the atmosphere. Winds occur on a wide range of temporal and spatial scales, associated with weather systems, storms, or fronts that are of great importance for meteorological forecasting (Goody and Walker, 1972). To advance the understanding of dynamic wind systems and improve the quality of operational weather forecasts at all scales and latitudes, the highest priority is given to observing wind profiles at the global scale (WMO, 1996). The current Global Observing System (GOS) is heavily biased towards mass observations, mainly provided by passive satellite instruments (Baker *et al.*, 2014). Information about the wind field can only be derived indirectly from these observations using the geostrophic approximation. However, this approximation is particularly limited at all scales in the Tropics, and at the mesoscale in the extratropics. Direct measurements of wind profiles from radiosondes, wind profilers, or commercial aircraft ascents and descents are relatively accurate but mainly concentrated on the continents of the Northern Hemisphere. Only few wind profiles are available over the oceans and on the Southern Hemisphere. Nearly globally distributed single-level winds can be derived from tracking cloud and water vapor structures in consecutive satellite images (atmospheric motion vectors [AMVs]), but they exhibit significant systematic and correlated errors due to uncertainties in their height assignment (Bormann *et al.*, 2003; Folger and Weissmann, 2014). The European Space Agency's (ESA's) Doppler wind lidar (DWL) satellite mission Aeolus, launched in August 2018, provides a novel dataset of wind profiles with quasi-global coverage that are an important recent supplement to the GOS. The atmospheric laser Doppler instrument (ALADIN) onboard the Aeolus satellite is the first DWL in space and should pave the way for future operational meteorological satellites dedicated to observing the atmospheric wind fields (ESA, 2008). Several theoretical and campaign-based studies investigated the potential impact of spaceborne DWL observations for NWP (e.g., Horányi *et al.* (2015a); Horányi *et al.* (2015b); Marseille *et al.* (2008b); Pu *et al.* (2010); Stoffelen *et al.* (2006); Tan *et al.* (2007); Tan and Andersson (2005); Weissmann *et al.* (2012); Weissmann and Cardinali (2007); Žagar (2004); Zhang and Pu (2010)), which showed that improvements are particularly expected in the initial atmospheric state in the Tropics and the Southern Hemisphere, in the forecast quality of the upper tropospheric and the lower stratospheric flow, and for short-range forecasts of severe weather situations and medium-range forecasts for the extratropical region.

The Aeolus satellite flies approximately 320 km above the Earth's surface in a polar sun-synchronous orbit and is tilted 35° towards the night side of the Earth. Within a repeat cycle of 7 days, which corresponds to 111 orbits, the satellite covers nearly the whole globe. The Aeolus direct detection wind lidar ALADIN, which operates in the ultraviolet spectral region (354.8 nm), probes the lowermost 17–25 km of the atmosphere by measuring the backscattered signals from both molecules (Rayleigh channel) and particles (Mie channel). This complementarity allows for broad vertical and horizontal data coverage of the line-of-sight winds (ESA, 2008; Reitebuch, 2012).

A crucial prerequisite to assimilate these novel meteorological observations in NWP data assimilation systems is a good knowledge of their statistical errors and the mitigation of systematic observation errors (Martin *et al.*, 2021). For this purpose, Aeolus level-2B (L2B) winds have been validated through extensive comparisons with reference datasets, such as ground-based radar wind profilers (Geiß *et al.*, 2020; Belova *et al.*, 2021), ground-based lidars (Baars *et al.*, 2020; Khaykin *et al.*, 2020), radiosondes (Baars *et al.*, 2020; Martin *et al.*, 2021; Liu *et al.*, 2022), and NWP model equivalents (Martin *et al.*, 2021; Rennie *et al.*, 2021). Further, airborne validation campaigns were performed, deploying the ALADIN Airborne Demonstrator and a 2  $\mu\text{m}$  DWL as reference (Lux *et al.*, 2020; Witschas *et al.*, 2020). The results of these studies provided the basis for an improved processing of the observations that reduces systematic errors and bias-correction schemes that can be applied during the assimilation.

In the year 2020, the European Centre for Medium-Range Weather Forecasts (ECMWF), the Deutscher Wetterdienst (DWD), Météo-France, and the UK's Meteorological Office started to assimilate Aeolus horizontal line-of-sight (HLOS) winds operationally. Several observing system experiment (OSE) studies have been conducted to investigate the impact of Aeolus in various NWP models. Garrett *et al.* (2022); Laroche and St-James (2022); Pourret *et al.* (2022), and Rennie *et al.* (2021) showed statistically significant improvements in short-range forecasts verified with other operational observing systems. Laroche and St-James (2022) found an enhanced forecast impact of HLOS winds in the Environment and Climate Change Canada (ECCC) global forecast system when AMVs are not assimilated. Overall, largest forecast improvements are documented for the 2- to 3-day forecasts for wind and temperature in the tropical upper troposphere and lower stratosphere and the Southern Hemisphere. In these regions, ECMWF (Rennie *et al.*, 2021) and Météo-France (Pourret *et al.*, 2022) reported a  $\sim 2\%$  reduction in root-mean-square forecast error verified against operational analyses. A reduction of up to 4% was found at the National Oceanic

and Atmospheric Administration (NOAA) (Garrett *et al.*, 2022). Further improvements were demonstrated in polar regions (Rennie *et al.*, 2021; Laroche and St-James, 2022), with less pronounced improvements in the midlatitudes of the Northern Hemisphere.

The impact of a specific observational dataset depends on factors such as the NWP model, data assimilation method, and experimental set-up. To comprehensively assess the usefulness of the Aeolus data and future-based DWL observations, it is therefore important to evaluate the impact with different NWP systems. In this study, we performed an OSE for 3 months, from July 2020 to October 2020, to investigate the impact of Aeolus in the global Icosahedral Nonhydrostatic model (ICON) of the DWD. So far, the already published impact studies have used a model resolution coarser than 20 km and four-dimensional variational assimilation techniques. The two experiments of the OSE at DWD (one with and one without Aeolus) were conducted at the full operational model resolution (horizontal grid-spacing of 13 km), applying the 3D hybrid variational ensemble Kalman filter (VarEnKF) scheme (Rhodin, 2015) with separate ensembles for the two experiments. They are based on the general operational settings, and all observation systems of the operational global NWP system of the DWD are assimilated.

The remainder of the study is structured as follows: Section 2 describes the Aeolus HLOS wind observations, the DWD assimilation system, the experiments conducted, and verification methods. Section 3 analyzes the data quality consistency of the assimilated Rayleigh and Mie HLOS winds using NWP model equivalents. Section 4 provides a statistical assessment of the impact of Aeolus on analyses and forecasts. The forecast verification is conducted using a selection of conventional observation types assimilated in the DWD system as well as the independent ECMWF Reanalysis v5 (ERA5) that did not assimilate Aeolus. Finally, Section 5 summarizes the main conclusions of the study.

## 2 | DATA AND METHODS

### 2.1 | The Aeolus L2B data

A comprehensive overview of all Aeolus data products and scientific data processing is provided in the ADM-Aeolus Science Report (ESA, 2008). The Aeolus L2B wind product, suitable for assimilation in NWP, contains the profiles of the HLOS wind observations of the Rayleigh and Mie channels. Since the ALADIN instrument points perpendicular to the relative velocity between the satellite and the Earth, the HLOS measurements outside the polar

regions correspond mainly to the zonal wind component, whereas the information about the meridional wind component dominates near the poles. A detailed description of the algorithms developed for the wind profile retrievals is provided by Tan *et al.* (2008). As a key step, the algorithms account for temperature and pressure broadening effects in the molecular backscatter signal by using NWP estimates of atmospheric temperature and pressure from a short-range forecast (Rayleigh–Brillouin correction) (Dabas *et al.*, 2008). Each measurement is derived from 20 accumulated laser pulse returns, corresponding to a horizontal resolution of about 2.9 km (Reitebuch *et al.*, 2020). In order to achieve a sufficient signal-to-noise ratio and to create representative averages within an observation, the measurements are grouped according to a scene-classification procedure (Tan *et al.*, 2008). The horizontal resolution of the resulting HLOS wind observations is typically about 90 km for the Rayleigh channel and 10 km for the Mie channel. The measurements within an observation are classified into an observation type, clear or cloudy, using measurement-scale optical properties; for example, the estimated particle scattering ratio or cloud information from the Mie channel (L1B Mie signal-to-noise ratio). Owing to the dual-channel receiver and the classification performed, four HLOS wind observation products are available: Rayleigh-clear, Rayleigh-cloudy, Mie-clear, and Mie-cloudy. In addition, the L2B processor provides several output data, such as an observation error estimate and quality flags for the wind observations that are useful for data assimilation systems. The accuracy of the Aeolus wind observations depends mainly on the intensity of the backscattered laser signal. In the Rayleigh channel, the concentration of atmospheric molecules and the presence of overlying clouds and aerosols determine the backscattering. In clear-sky conditions, the Rayleigh wind coverage reaches up to about 30 km from the surface. The Mie channel analyzes the particle backscatter signal from clouds and aerosols. It is strongest within optically thin clouds and on top of optically thick clouds. Weaker Mie signals come from the planetary boundary layer and from aerosol layers in clear-sky conditions. Within and below optically thick clouds, the laser signal is totally attenuated. The Aeolus HLOS wind observations are accumulated in 24 vertical bins, varying from 0.25 km near the surface to 2 km in the highest bins. The range bin settings along the orbit can be adjusted in order to achieve the best NWP impact or for the investigation of specific atmospheric phenomena; for example, atmospheric waves (Rennie *et al.*, 2021).

During the mission, the laser instrument performance, and thus the data quality, varied considerably. Further, the Aeolus processing algorithms have evolved and were refined since the satellite launch in 2018. The essential

changes in the Aeolus L2B dataset for near-real-time operational processing during the mission up to April 2020 are described in Rennie and Isaksen (2020). The Aeolus data used in this study are within the processor baseline 2B10 period. The main improvement in 2B10 with respect to the original processor baseline is a near-real-time correction of the HLOS wind bias in the L2B product using a linear correlation between  $O - B$  (observation minus background) statistics from ECMWF and temperatures from the telescope primary mirror M1. More details about the M1-mirror-temperature-dependent bias correction can be found in Rennie *et al.* (2021) and Weiler *et al.* (2021). Rennie *et al.* (2021) also showed improvements in NWP impact at ECMWF due to the optimized processor baseline. However, small residual biases may still occur at the regional level.

## 2.2 | Model and experimental design

The global NWP model ICON at DWD is based on the non-hydrostatic system of equations in the global domain (Zängl *et al.*, 2015). In the current operational version, the atmosphere is resolved by an icosahedral grid of approximately 13 km horizontal mesh size and 90 terrain-following model levels extending from the surface to a height of 75 km. The core module of the global data assimilation system is a VarEnKF, which consists of a local ensemble transform Kalman filter (LETKF) and a 3D variational (3DVar) data assimilation system (Rhodin, 2015). The VarEnKF combines the localized ensemble background error covariance matrix from the LETKF  $\mathbf{P}_{\text{EnKF}}^b$  with the static 3DVar covariance matrix  $\mathbf{P}_{\text{static}}^b$  used formerly in the 3DVar:

$$\mathbf{P}^b = \alpha \mathbf{P}_{\text{EnKF}}^b + \beta \mathbf{P}_{\text{static}}^b, \quad \alpha + \beta = 1. \quad (1)$$

In the DWD hybrid data assimilation system, the weights are  $\alpha = 0.7$  and  $\beta = 0.3$ . This combination consistently considers temporal background error covariances with the model dynamics, generating a stable analysis state that incorporates more information from the observations than the pure 3DVar could (Reinert *et al.*, 2023). The LETKF is based on a 40-member ensemble with a lower resolution of 40 km and a horizontal localization radius of 300 km. The assimilation is carried out with a 3 hr cycling (0000, 0300, ..., 1800, 2100 UTC). A 3-hr short-term forecast serves as background field that is adjusted using all observations within  $\pm 1.5$  hr around the corresponding time step to generate the analysis field from which the next forecast is initialized.

The zonal and meridional components of the model background winds  $u$  and  $v$  are transformed to the Aeolus

**TABLE 1** The assigned observation error  $\sigma(\epsilon_{O\_ass})$  in the observing system experiment for specific pressure levels.

Level (hPa)	$\sigma(\epsilon_{O\_ass})$ (m·s <sup>-1</sup> )
1,000	5.50
850	5.00
700	4.50
500	4.50
400	4.75
300	5.00
250	5.00
200	5.25
150	5.25
100	5.50
70	6.00
50	6.50
30	7.00
20	7.50
10	8.00

HLOS wind equivalent using the following observation operator:

$$\text{HLOS} = -u \sin \phi - v \cos \phi, \quad (2)$$

where  $\phi$  is the satellite azimuth angle that represents the laser's line-of-sight projected onto the horizontal plane, being typically  $\sim 260^\circ$  for ascending orbits and  $\sim 100^\circ$  for descending orbits. Vertical averaging is not included in the observation operator. The model background winds  $u$  and  $v$  are interpolated to the Aeolus observation geolocation point (latitude, longitude, and height). Thus, the HLOS winds are assumed to be point observations with neglected vertical velocity. This is a reasonable approach, as the effective resolution of the global ICON model is between 80 and 100 km in the horizontal and between a few hundred meters (lower troposphere) up to 2 km (stratosphere) in the vertical, which is similar to the averaging length scale of Rayleigh HLOS winds but slightly larger than the averaging length of Mie winds. The assigned observation error  $\sigma(\epsilon_{O\_ass})$  was derived based on the Desroziers method (Desroziers *et al.*, 2005) and is used in a table-driven format for specific pressure levels (Table 1). Between these levels it is interpolated.

In the OSE, two continuous assimilation cycles were performed based on the operational version of the ICON model at its full resolution: a "control" run without the Aeolus but with all other operationally used observation types assimilated (CTRL), and an experiment with the Rayleigh and Mie HLOS wind observations assimilated

in addition to all other observation types (EXP\_A). Both assimilation experiments were conducted with a corresponding cycled LETKF ensemble run. Within the 3-hr assimilation window, more than 600,000 observations are operationally assimilated at DWD, the majority being radiances (~64% of the total observations). Winds from scatterometers, satellite imagery, and Global Navigation Satellite System (GNSS) signals together constitute about 18%. Conventional observations from aircraft reports, radiosondes, surface stations, buoys, pilot, and wind profilers represent ~7% of the total number of observations. For EXP\_A, only Rayleigh-clear or Mie-cloudy winds with a valid confidence flag were used as they are the highest quality L2B wind products (from now on, referred to as Rayleigh and Mie). The proportion of assimilated wind profiles from the spaceborne lidar of the Aeolus mission in EXP\_A is about 2%. Low-level Rayleigh winds with a range-bin thickness of 0.25 km were rejected due to noise and atmospheric attenuation in the boundary layer. Furthermore, specific thresholds of the L2B processor estimated error were chosen to find a compromise between the quality of the dataset and the number of observations that pass the quality control. Therefore, Rayleigh winds with an estimated error greater than  $8 \text{ m}\cdot\text{s}^{-1}$  and Mie winds with an estimated error greater than  $6 \text{ m}\cdot\text{s}^{-1}$  were excluded. A bias correction was applied to the Rayleigh and Mie wind observations to remove a systematic height-dependent error (see Section 3) and thus optimize the assimilation performance. The bias correction is a function of latitude and height, with the latter divided into specific levels: surface–850 hPa, 850–500 hPa, 500–200 hPa, 200–70 hPa, 70–5 hPa. The correcting function is based on the previous 7 days and applied to the Rayleigh HLOS winds separately for ascending and descending orbits. The choice of bias correction generally differs between the Aeolus OSEs performed at different NWP centers. At ECMWF (Rennie *et al.*, 2020) and ECCO (Laroche and St-James, 2022), no bias correction was applied in addition to the operationally implemented M1-mirror-temperature-dependent bias correction. Pourret *et al.* (2022) used a correction method for the Rayleigh clear winds developed at Météo-France, which is based on a temporal and spatial statistical comparison between good-quality Rayleigh cloudy and Mie cloudy data. At NOAA (Garrett *et al.*, 2022), a total least-squares regression analysis of the discrepancies between Aeolus and the model's background winds was used to correct for the bias. Similar to this study, it is based on the winds of the previous 7 days and depends on latitude, altitude, and orbit phase. The bias correction approach applied within the OSE of this study is mainly based on a previous study of Aeolus bias correction approaches (Martin *et al.*, 2021).

## 2.2.1 | Verification data and method

To assess the impact of the Aeolus observations, analysis fields and forecast errors of the CTRL and EXP\_A experiment are compared. A forecast error is the difference between the forecast and the true atmospheric state. Typically, either NWP analyses at the time the forecast is valid or a statistically significant sample of observational data of other observation types are used to represent a reliable proxy for the “truth”. However, it should be noted that these proxies contain their own errors depending on the choice of the verification data. For example, the error of short-range forecasts up to 36 hr is likely correlated with that of the analysis leading to potential systematic errors in such a verification, especially if the same modeling system is used (Geer *et al.*, 2010). In this study, we verified short-term forecasts up to 36 hr against measurements from a selection of other observation types (radiosondes, aircraft, GNSS radio occultations [GNSS-ROs], and AMVs) by comparing the root-mean-squared error (RMSE) of  $O - B$  values. These observations are, to a large extent, independent of the evaluated forecasts. In the case of biases, however, the verification results may be influenced by them. For the verification of longer forecast lead times, ERA5 data are used as independent analyses. ERA5 is produced using the four-dimensional variational data assimilation and model forecasts of the ECMWF Integrated Forecasting System (IFS) with a horizontal resolution of 31 km. Besides the different model and resolution, ERA5 also assimilates a different set of observations compared with the ICON system; for example, a larger number of satellite observations. Furthermore, ERA5 is entirely independent of Aeolus, as those data were not assimilated therein.

The forecast error of an experiment  $X$  is calculated as

$$e_i^X = \text{forecast}_i^X - \text{truth}_i^Y. \quad (3)$$

For this study,  $X$  is either the CTRL or the EXP\_A run,  $Y$  is the verification data representing the “truth” (observation or ERA5 data), and  $i$  is the time step when the forecast and analysis are valid. The RMSE of the experiment  $X$  determines how strongly the forecast deviates from the verification data:

$$\text{RMSE}(e^X) = \sqrt{(e_i^X)^2}. \quad (4)$$

Depending on the quantity of interest, the mean – denoted by the overbar in Equation (4) – is either calculated over time, pressure level, latitude or longitude, or over several dimensions. The normalized differences in RMSE between EXP\_A and CTRL then provide the improvement/degradation in forecast quality due to the Aeolus observations

by negative/positive values respectively:

$$e_{\text{diff}} = \frac{\text{RMSE}(e^{\text{EXP\_A}}) - \text{RMSE}(e^{\text{CTRL}})}{\text{RMSE}(e^{\text{CTRL}})}. \quad (5)$$

### 3 | DATA QUALITY AND CONSISTENCY OF THE AEOLUS HLOS WINDS

#### 3.1 | Systematic observation errors

To evaluate the error characteristics of the Aeolus data in the OSE time period, first, the HLOS wind observations  $O$  are compared with the short-range forecast model equivalent HLOS winds  $B$ . Averaged over large spatial and time scales, the model bias is generally small compared with that of the Aeolus observations, so that the systematic observation errors can be estimated by the mean  $O - B$  departures (innovations). Figure 1 shows the mean  $O - B$  departures on a global scale as a function of altitude for both Rayleigh and Mie HLOS winds for the period July 1, 2020, to September 30, 2020, for ascending and descending orbits. Despite the operational telescope M1-mirror-temperature dependent bias correction (Section 2.1), which leads to a large improvement in the HLOS wind data quality (Rennie *et al.*, 2021), a remaining bias with negative values in the troposphere and positive

values around the tropopause and in the lower stratosphere is apparent for the Rayleigh wind observations (Figure 1a,b). The height dependency is assumed to be related to the atmospheric background temperature used for the Rayleigh–Brillouin correction (Šavli *et al.*, 2021). The investigation of this effect is, however, still ongoing. In total, the magnitude of the mean  $O - B$  departure is small ( $< \pm 1 \text{ m}\cdot\text{s}^{-1}$ ), indicating that the M1-mirror-temperature dependent bias correction performs reasonably well. To further optimize the Aeolus HLOS winds for their assimilation in the ICON model, an additional model-based bias correction was applied for the OSE (Section 2.2). For levels below 500 hPa and above 200 hPa, this bias correction reduces the differences between Aeolus winds and NWP model background winds to almost zero, thus eliminating the height dependency of the bias. On average, the residual absolute systematic deviations are about  $0.2 \text{ m}\cdot\text{s}^{-1}$ ; that is, half as large as without the model-based bias correction. The Mie bias is not as much related to the atmospheric background temperature and is therefore not as sensitive to temperature variations with altitude. After the M1-mirror-temperature-dependent bias correction, the additional model-based bias correction did not improve the Mie HLOS winds further. Whereas the Aeolus Rayleigh wind bias does not differ significantly between ascending and descending orbits, the Aeolus Mie bias (Figure 1c) exhibits a dependence on the orbit phase. A similar pattern has been seen in the weekly monitoring

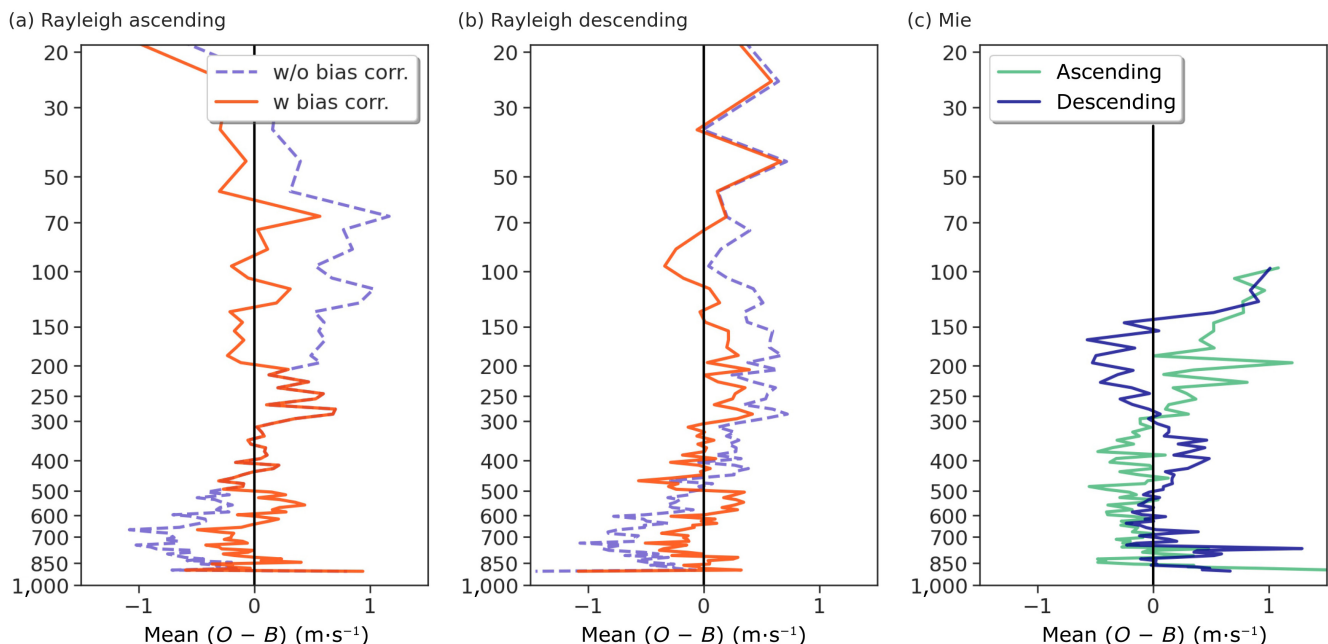


**FIGURE 1** Mean observation  $O$  minus background  $B$  departures (bias) as a function of pressure (hPa) of the Aeolus horizontal line-of-sight (HLOS) Rayleigh winds for (a) ascending and (b) descending orbits for July 1, 2020, to September 30, 2020 – without bias correction (purple dashed line) and with bias correction (orange solid line) – and (c) for the Aeolus HLOS Mie winds separately for ascending (cyan) and descending (blue) orbits. [Colour figure can be viewed at [wileyonlinelibrary.com](https://onlinelibrary.wiley.com/terms-and-conditions)]

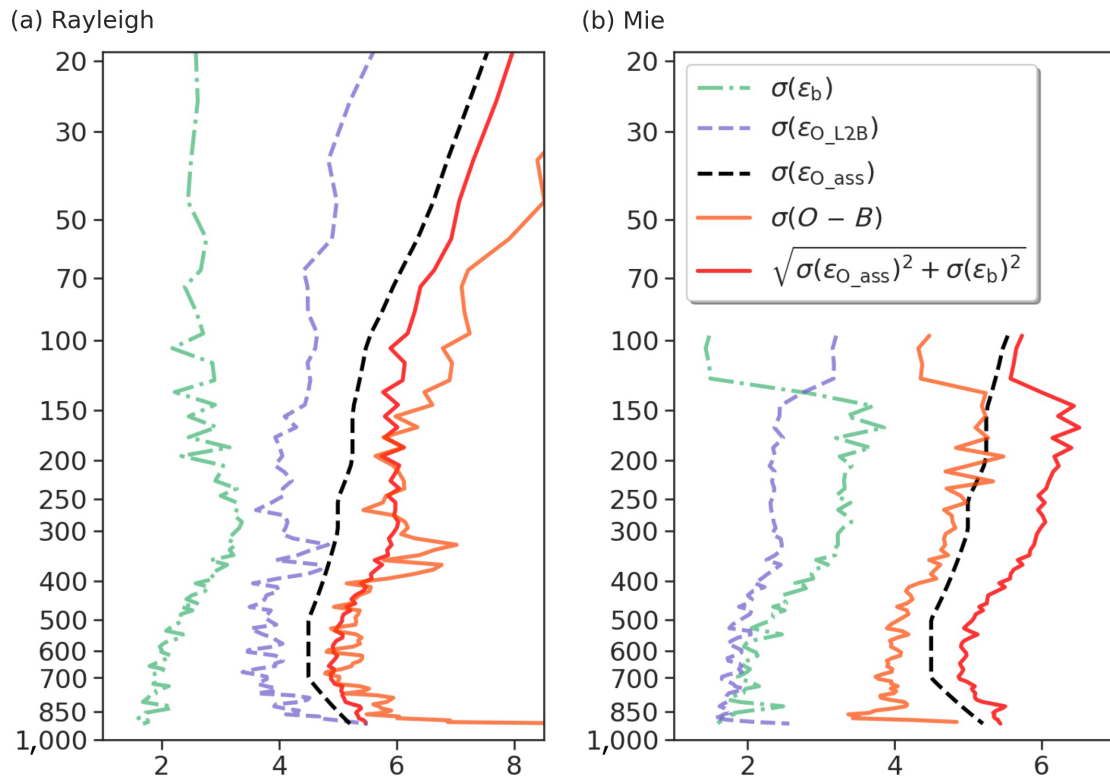


**FIGURE 2** Random error estimates of the Aeolus horizontal line-of-sight (a) Rayleigh and (b) Mie winds as a function of pressure (hPa) for July 1, 2020, to September 30, 2020, including the background error  $\sigma(\epsilon_b)$  (green), the level-2B (L2B) estimated observation error  $\sigma(\epsilon_{O\_L2B})$  (purple), the assigned observation error  $\sigma(\epsilon_{O\_ass})$  (black), the standard deviation of the observation  $O$  minus background  $B$  departures  $\sigma(O - B)$  (orange), and the random error estimate when combining  $\sigma(\epsilon_{O\_ass})$  and  $\sigma(\epsilon_b)$  (red). [Colour figure can be viewed at [wileyonlinelibrary.com](https://onlinelibrary.wiley.com/doi/10.1002/qj.4541)]

routine at ECMWF (ECMWF, 2023), suggesting that these systematic errors are Aeolus and not model biases. According to Marseille *et al.* (2022), the systematic Mie errors are due to imperfections of the data in the absolute instrument calibration tables, which serve as input for the on-ground wind-processing algorithms. An updated calibration table for the Mie channel based on NWP model winds that reduces the bias and has become part of the operational processing chain since July 1, 2021. However, the processor baseline used for the OSE is an older version, and the magnitude of the bias of the assimilated Mie winds is between  $-0.8$  and  $+1.2 \text{ m}\cdot\text{s}^{-1}$  for descending orbits and between  $-0.5$  and  $+0.7 \text{ m}\cdot\text{s}^{-1}$  for ascending orbits. The absolute systematic error of Mie winds is about  $0.2 \text{ m}\cdot\text{s}^{-1}$  for ascending orbits and  $0.3 \text{ m}\cdot\text{s}^{-1}$  for descending orbits.

### 3.2 | Random observation error estimates

Figure 2 displays the random error estimates as a function of altitude, including the observation error provided by the L2B processor  $\sigma(\epsilon_{O\_L2B})$ , the observation error assigned

in the assimilation  $\sigma(\epsilon_{O\_ass})$  (Section 2.2), and the standard deviation of the  $O - B$  departures  $\sigma(O - B)$ . The latter consists of the random error estimate of the Aeolus winds  $\sigma(\epsilon_O)$  and the background error  $\sigma(\epsilon_b)$ :

$$\sigma(O - B) \approx \sqrt{\sigma(\epsilon_O)^2 + \sigma(\epsilon_b)^2}. \quad (6)$$

Together with the assigned observation error, the background error determines how closely the analysis field is drawn to the Aeolus observations compared with the background. Low assigned observation errors and large model errors allow Aeolus wind observations to have a more significant impact. Overall, the Aeolus random errors are relatively large and beyond the mission requirements (ESA, 2016). In the OSE, the assigned observation error is the same for both Rayleigh and Mie observations and generally increases with altitude. The background error is largest at around 150 hPa for Mie wind model equivalents and around 300 hPa for Rayleigh wind model equivalents. The assigned observation error is generally larger than the observation error estimated by the L2B processor, which does not include the uncertainties due to representativeness. These differences are more pronounced for Mie winds than for Rayleigh winds. However, the

increase of  $\sigma(\epsilon_{O\_ass})$ ,  $\sigma(\epsilon_{O\_L2B})$ , and  $\sigma(O - B)$  with height agree relatively well, indicating a higher precision of Aeolus observations in the midtroposphere compared with upper levels. Both the Rayleigh estimated L2B error and the standard deviation of  $O - B$  departures appear to be increased at pressure levels between 300 and 400 hPa (the large values near the surface are due to the small sample size in the bottom bin). In summer 2020, the general tropical range-bin setting in the Tropics  $\pm 30^\circ$  latitude and the range-bin setting in the extratropics  $> 30^\circ$  N and between  $-30^\circ$  and  $-60^\circ$  S was adjusted by increasing the vertical sampling around the jet stream between 5 and 10 km. Improvements from the optimized range-bin setting are mainly expected from the higher number of Mie observations, since clouds usually generate high levels of noise at these altitudes. Since the random errors of the Rayleigh winds depend on the atmospheric path signal and are therefore affected by the signal accumulation (vertical and horizontal), the increased values between 300 and 400 hPa are probably related to these smaller range bins.

For a consistency check on how well the assigned observation error represents  $\sigma(\epsilon_O)$  in the assimilation system, it is combined with the background error as follows:

$$\sigma_{\text{consistency\_check}} = \sqrt{\sigma(\epsilon_{O\_ass})^2 + \sigma(\epsilon_b)^2}. \quad (7)$$

Ideally, this corresponds to the standard deviation of the  $O - B$  departures. The profiles of  $\sigma(O - B)$  and  $\sigma_{\text{consistency\_check}}$  match quite well for Rayleigh winds, except for small discrepancies in the discussed levels with increased vertical resolution and above the tropopause, where either the assigned observation error or the ensemble spread is too small. The Mie winds show deviations of about  $1 \text{ m}\cdot\text{s}^{-1}$ , indicating that slightly too low a weight is assigned to them. Usually, the Mie observations tend to be more precise than Rayleigh observations because the backscatter signal from clouds is about an order of magnitude larger than during clear-sky conditions, and Mie observations are not affected by Doppler broadening due to Brownian motion. A variational quality control (VarQC), as included in the DWD assimilation system, can partly compensate for inconsistencies of the assigned observation error. VarQC operates during the iterative minimization as part of the solution of the variational problem and reduces the weight of observations with large deviations compared with the statistical expectation. It is more active for observations with low assigned errors and less active in the case of large assigned errors. Therefore, the resulting VarQC weight of Rayleigh winds was smaller than that of Mie winds (not shown). Overall, the data quality and monitoring statistics are fairly constant throughout

the OSE period, which is why time series are not displayed here.

## 4 | ASSESSMENT OF NWP IMPACT OF AEOLUS HLOS WINDS

### 4.1 | Systematic changes in the analysis

Figure 3 shows the systematic changes in the analysis of the zonal wind component due to the assimilation of Aeolus observations ( $EXP\_A - CTRL$ ) for 100, 250, and 600 hPa. Positive values indicate that Aeolus observations tend to make the zonal wind component more westerly. Negative values indicate a strengthening of easterly flow. Additionally, the absolute mean analysis differences between the CTRL run of the OSE and ERA5 are shown, providing a qualitative estimate of the structure of systematic analysis uncertainties. Altogether, the most pronounced systematic influence of the Aeolus observations occurs around key atmospheric circulation systems, strong large-scale wind regimes, and convectively active areas in the Tropics, where uncertainties in the analysis are systematically larger, and the background forecast does not represent the associated atmospheric phenomena well.

In the midtroposphere, the trend of making the zonal wind more westward is strongest around the Indian Ocean and slightly less above the West Pacific and the East Pacific Ocean south of the Equator. West winds are accelerated in the equatorial East Pacific. The strengthening of easterlies around the west coast of Africa is probably related to the mid-level African easterly jet, which was found to be strongly influenced by the Aeolus HLOS winds, especially the northern part (Borne *et al.*, 2022). Uncertainties in the Indian Ocean are likely to be associated with the synoptic-scale monsoon circulation system in the lower troposphere, which typically lasts from June to September.

At 250 hPa, the Aeolus observations largely influence the zonal wind field in the East Pacific, where systematic analysis uncertainties are also increased. Changes in the analysis due to the assimilation of HLOS winds occur as strengthening of easterlies. These changes in the upper level are presumably related to modifications in the zonal Walker circulation, which in turn is connected to the state of El Niño–Southern Oscillation (ENSO). The state of ENSO switched during the OSE period, so we assume that associated changes in the convective pattern at the coast of South America and Indonesia are the dynamical source of the strong influence. Furthermore, enhanced influence of Aeolus observations in the upper troposphere is found in the mid-Atlantic Ocean and the polar regions, but with fluctuations in sign of the mean differences.

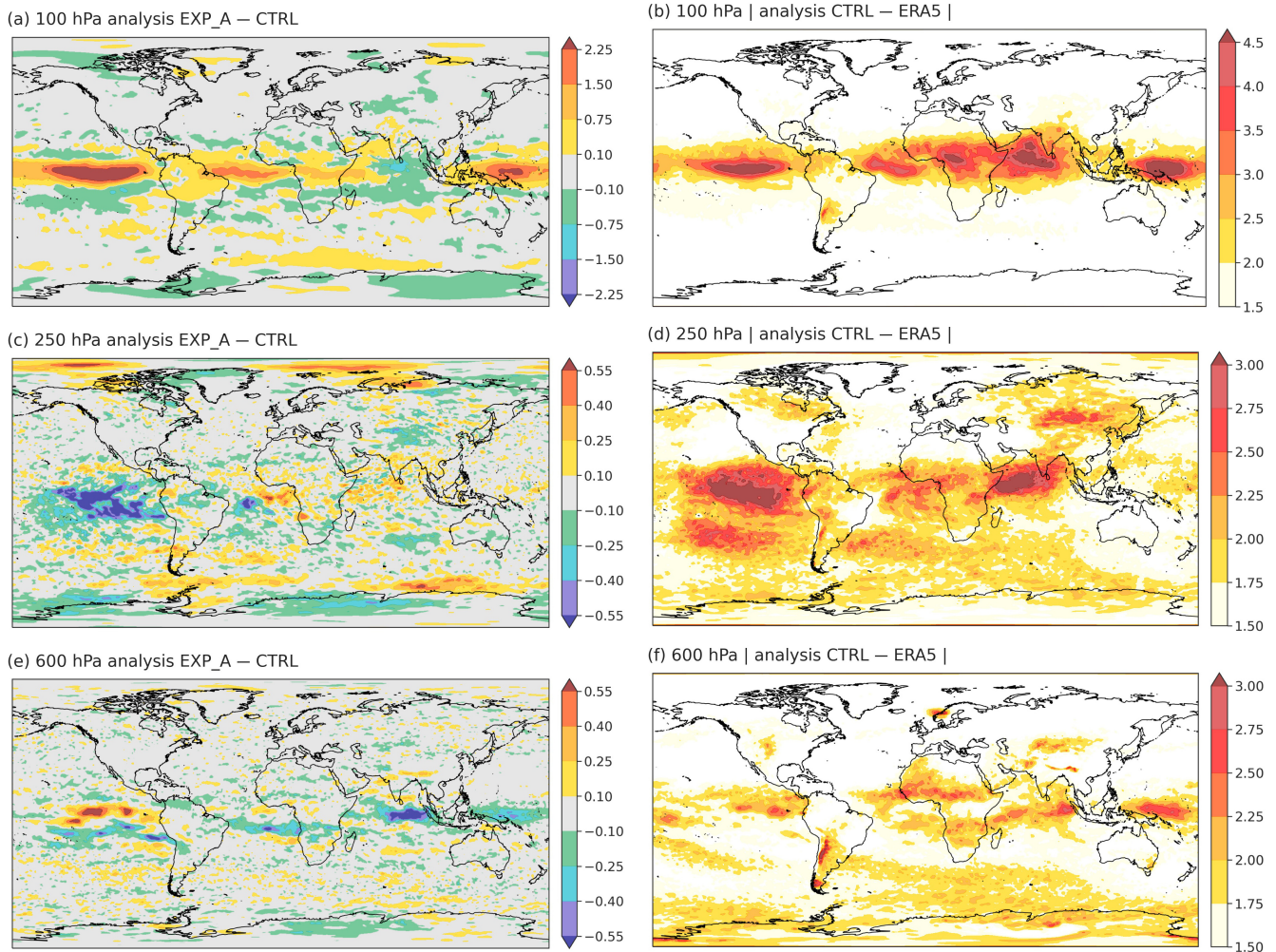


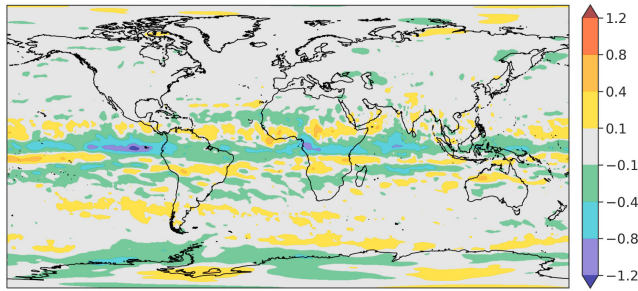
**FIGURE 3** Mean analysis difference ( $EXP\_A - CTRL$ ) of (a, c, e) the zonal wind component  $U$  and (b, d, f) absolute mean difference of the zonal wind component between the CTRL analysis and the European Centre for Medium-Range Weather Forecasts Reanalysis v5 (ERA5) at (a, b) 100 hPa, (c, d) 250 hPa, and (e, f) 600 hPa for July 1, 2020, to September 30, 2020. Note different color scales for 100 hPa compared with 250 and 600 hPa. [Colour figure can be viewed at [wileyonlinelibrary.com](https://onlinelibrary.wiley.com/terms-and-conditions)]

At the level of the tropical tropopause, the mean zonal wind analysis is particularly modified around the Equator (note that the color scale is different from the lower levels; Figure 3c,e). There, the strengthening of westerlies dominates. Only at the edge of the Tropics and above the Indian Ocean are easterly winds accelerated when including the Aeolus observations. The analysis changes in the surrounding of the Indian Ocean probably represent an amplification of the upper level tropical easterly jet that develops in the upper atmosphere during the Asian monsoon. Compared with the ERA5, the tropical easterly jet region is characterized by large systematic analysis uncertainties. Besides the Tropics, an influence of the Aeolus observations is again visible in the Southern Hemisphere's polar region.

Since the pattern of changes in the mean zonal wind analysis due to Aeolus is quite constant with time in the troposphere, we concentrated on the mean over

the whole OSE period. The picture looks different at the stratospheric levels. Figure 4 shows the same as Figure 3a,c,e, but separately for (a) July to mid-August and (b) mid-August to September at 50 hPa. Between 70 and 10 hPa, typically, the quasi-biennial oscillation (QBO) of the equatorial zonal wind between easterlies and westerlies takes place by downward propagation of the successive wind regime with a period of 22–34 months. In winter 2019–2020, the QBO phase change from westerly to easterly winds was disrupted, and an eastward zonal-mean jet subsequently emerged above the shallow westward layer (Anstey *et al.*, 2021). In 2020 the normal QBO cycling manifested again as a westerly jet. The OSE period covers the alternation between 50 and 30 hPa, where the QBO westerly phase evolved mid-August. In the time before the emergence of the westerly jet at 50 hPa (Figure 4a), the Aeolus observations tend to accelerate the easterlies around the Equator. However, the

(a) 50 hPa: July 1, 2020–August 15, 2020



(b) 50 hPa: August 15, 2020–September 30, 2020

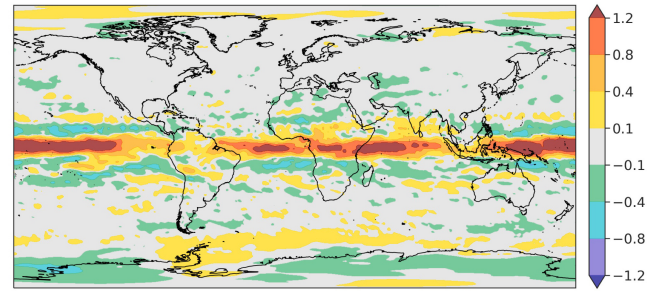
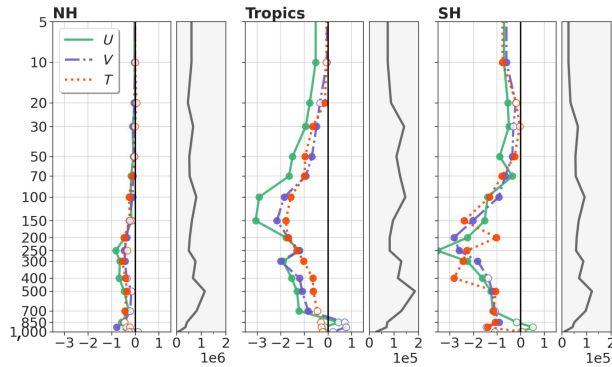
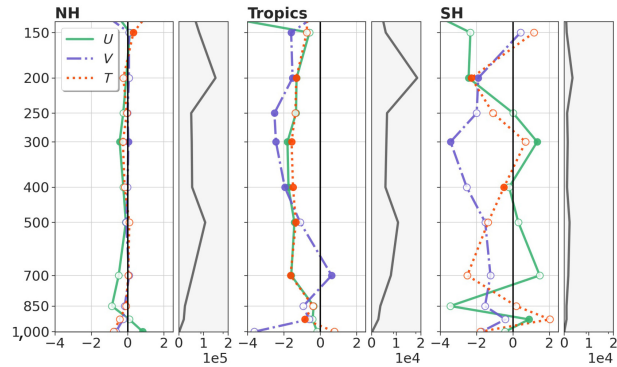


**FIGURE 4** Mean analysis difference ( $EXP\_A - CTRL$ ) of the zonal wind component  $U$  at 50 hPa for (a) July 1, 2020, to August 15, 2020, and (b) August 15, 2020, to September 30, 2020. [Colour figure can be viewed at [wileyonlinelibrary.com](https://onlinelibrary.com)]

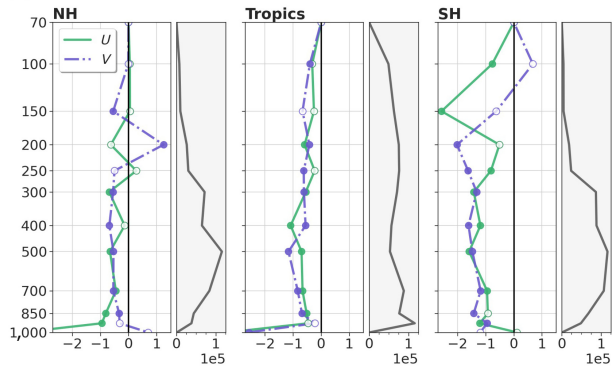
(a) TEMP



(b) AIREP



(c) AMV



(d) GNSS-RO

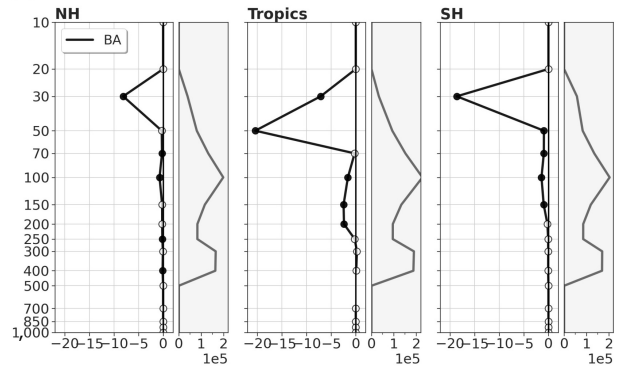


**FIGURE 5** The relative mean differences in root-mean-squared error (%) between the  $EXP\_A$  and the  $CTRL$  run along the forecast ranges between 3 and 36 hr as functions of altitude for July 1, 2020, to September 30, 2020, verified against (a) radiosonde (TEMP) and (b) aircraft report (AIREP) for the zonal  $U$  and meridional  $V$  wind components and the temperature  $T$ , against (c) atmospheric motion vector (AMV) for  $U$  and  $V$  and against (d) Global Navigation Satellite System radio occultation (GNSS-RO) observations for the bending angle (BA), separately for the Tropics, the Northern Hemisphere (NH), and Southern Hemisphere (SH). Filled circles indicate significant differences (95% confidence range, Student's  $t$ -test), empty circles indicate non-significant differences. The gray lines in the subplots alongside present the number of observations. [Colour figure can be viewed at [wileyonlinelibrary.com](https://onlinelibrary.com)]

magnitude of the influence is much weaker than in the second half of the OSE period, during the QBO westerly phase (Figure 4b). Those equatorial west winds are strengthened to a large extent by the Aeolus observation. The ability of Aeolus to measure this reversal is investigated in more detail elsewhere (Martin *et al.*, 2023).

## 4.2 | Short-range forecast impact: Observation-based verification

The impact of the Aeolus HLOS winds on the quality of short-range forecasts up to 36 hr is verified by the fit to observations from radiosondes (TEMP), aircraft (AIREP), GNSS-ROs, and AMVs. The relative mean differences in

**TABLE 2** Averaged values of differences in root-mean-squared error (%) between the EXP\_A and the CTRL run along the forecast ranges between 3 and 36 hr for July 1, 2020, to September 30, 2020, from Figure 5.

	Variable	Northern Hemisphere	Tropics	Southern Hemisphere
TEMP	<i>U</i>	−0.30	−1.20	−1.05
	<i>V</i>	−0.25	−0.70	−1.21
	<i>T</i>	−0.25	−0.69	−1.12
AIREP	<i>U</i>	−0.14	−1.07	−0.48
	<i>V</i>	−0.08	−1.57	−1.59
	<i>T</i>	−0.15	−0.99	−0.54
AMV	<i>U</i>	−0.46	−0.51	−0.70
	<i>V</i>	−0.12	−0.51	−0.75
GNSS-RO	BA	−0.59	−0.77	−1.36

Abbreviations: AIREP, aircraft report; AMV, atmospheric motion vector; BA, bending angle; GNSS-RO, global navigation satellite system radio occultation; *T*, temperature; TEMP, radiosonde; *U*, zonal wind component; *V*, meridional wind component.

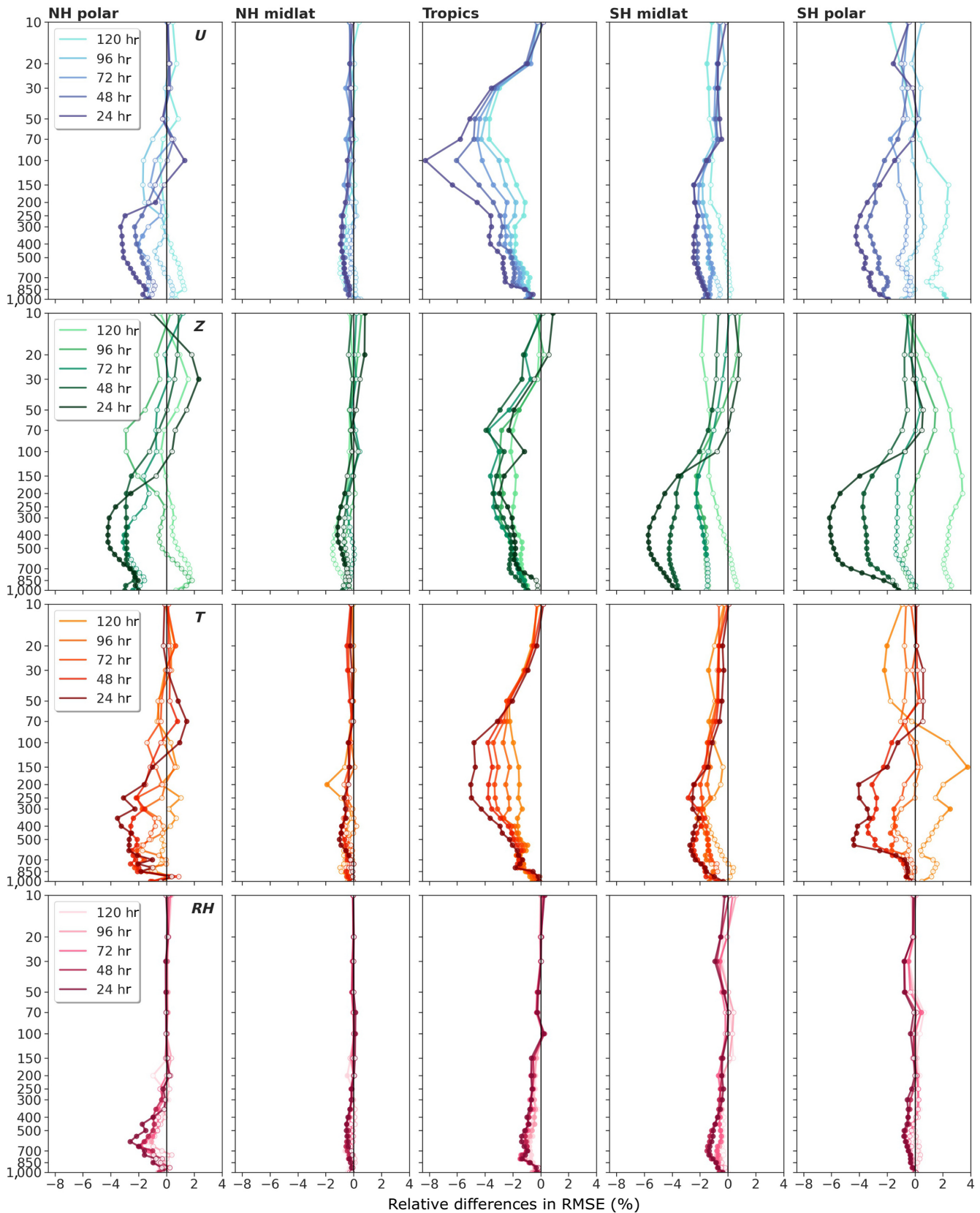
RMSE of  $O - B$  values between EXP\_A and the CTRL run as functions of altitude are shown in Figure 5, separately for the Tropics, the Northern Hemisphere, and the Southern Hemisphere. The size of each compared sample is presented by the gray line in the subplots alongside. Additionally, the average values of the changes in forecast error are listed in Table 2. Beneficial impact (represented by negative values) for radiosonde wind and temperature observations is largest in the Tropics and the Southern Hemisphere, with a maximum around the tropopause (up to 3.5% improvement). The Northern Hemisphere, where the number of radiosonde observations is highest, shows a smaller impact, but on average, up to 0.3% improvement is found that also peaks at heights of the extratropical tropopause. The fit to wind and temperature observations from aircraft, which are most frequent at flight levels, are also mainly improved in the Tropics (up to 1.6%) and to a lower extent in the Northern Hemisphere (up to 0.2%). The impact evaluation with respect to aircraft observations in the Southern Hemisphere suffers from a low number of measurements and is not significant for most levels. Thus, these results should be treated with caution. AMVs and GNSS-RO observations, in contrast, are quite abundant in the Southern Hemisphere. On average, the impact is 0.7% relative to AMV winds and 1.4% relative to bending angles from GNSS-RO measurements. The largest improvements for AMVs are found in the lower troposphere and midtroposphere, where the number of observations compared is highest. Around 400–500 hPa, the maximum impact in the Tropics is 1.2%. In the Northern Hemisphere, improvements of ~1% occur. GNSS-RO impact is strongest

in the mid- and lower stratosphere. At 30 hPa, the maximum is reaching 8% or even more. At lower levels, where the sample of observations compared is larger, the impact reaches up to 3% in the Tropics. In general, the changes in the short-range forecast errors resulting from assimilating Aeolus HLOS winds consistently show positive impact verified with radiosonde, aircraft, AMV, and GNSS-RO observations. The largest improvements are mainly found in upper atmospheric levels in the Tropics and the Southern Hemisphere, also depending on the number of measurements. Despite the good coverage of observations in the Northern Hemisphere, Aeolus HLOS winds nevertheless still have a comparably large impact on the short-range forecast there.

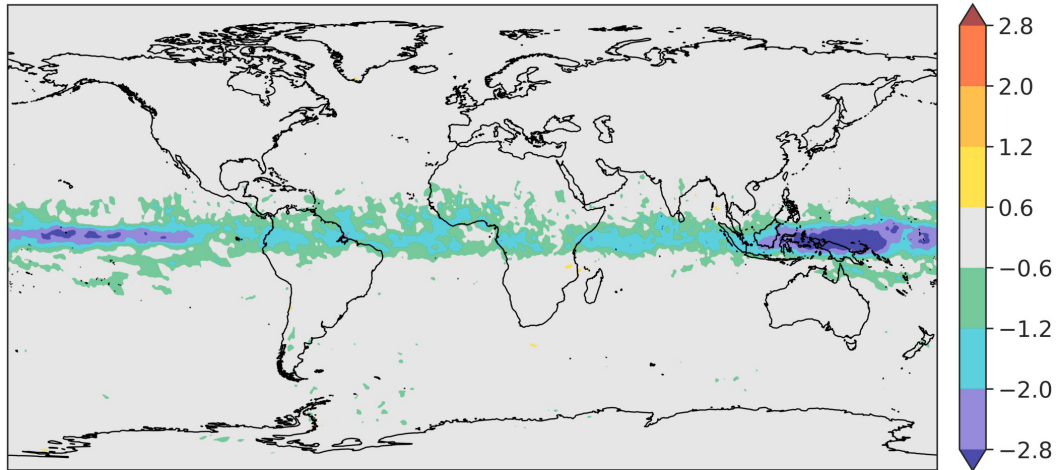
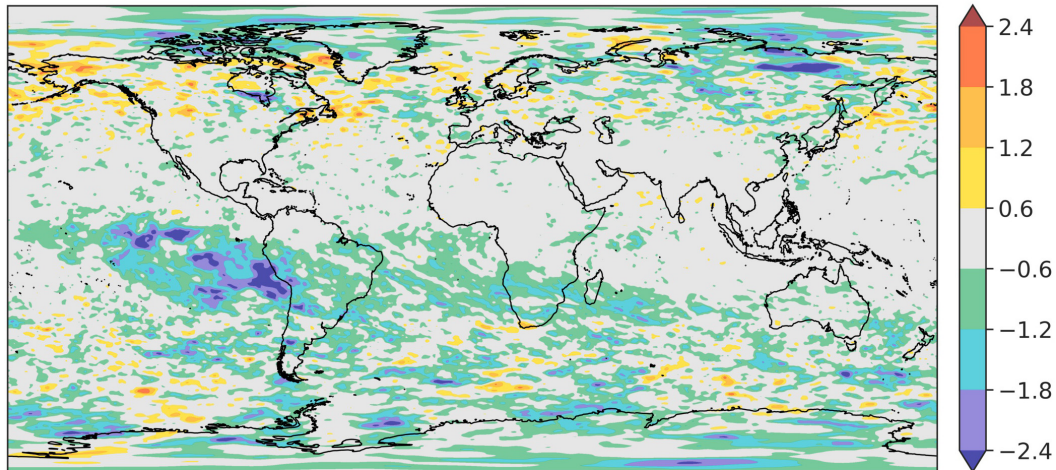
### 4.3 | Medium-range forecast impact: Analysis-based verification

To evaluate the impact of the Aeolus HLOS winds on forecasts with lead times of 24–120 hr, these forecasts are verified against ERA5. An overview of the forecast error reduction in terms of relative differences in RMSE between EXP\_A and the CTRL run for the Tropics, the midlatitudes, and the polar region of both hemispheres as a function of altitude is provided in Figure 6. The relative reduction of forecast error is shown for the zonal wind component (*U*), geopotential (*Z*), temperature (*T*), and relative humidity (RH). The impact on the meridional wind component (not shown) is similar to that for *U*. The verification with analyses can involve larger uncertainties for short lead times, as forecast errors strongly correlate with the analysis uncertainty, especially in data-sparse areas (Geer *et al.*, 2010). Therefore, results for 24 hr should be treated with caution.

As expected, and similar to the observation-based verification (Figure 5), Aeolus wind observations lead to the largest error reduction in the Tropics, where winds are not constrained by geostrophic balance. This is evident for all four variables and for all forecast lead times. For the zonal wind component, the forecast quality in the Tropics is improved by at least 2% and up to 8%, peaking at the tropopause height around 100 hPa. For temperature, the largest improvements in the Tropics are in the upper troposphere, for RH between 500 and 850 hPa. Overall, the gain in lead time in the Tropics is up to 6 hr (not shown here). Besides the Tropics, the forecast is, on average, also improved in polar regions and the midlatitudes of both hemispheres. In the Southern Hemisphere, significant beneficial impact of Aeolus is predominantly below the tropopause around the jet level and then decreases with altitude for forecast lead times of 24 to 72 hr. Only RH exhibits a second peak in the Southern Hemisphere in



**FIGURE 6** The mean relative differences in root-mean-squared error (RMSE; %) of zonal wind component ( $U$ ), geopotential ( $Z$ ), temperature ( $T$ ), and relative humidity ( $RH$ ) as function of pressure (hPa) for the Tropics, the midlatitudes (NH midlat, SH midlat), and polar region (NH polar, SH polar) for July 1, 2020 to September 30, 2020, as a function of altitude for forecast lead times from 24 hr up to 120 hr. Filled circles indicate significant differences (95% confidence range, Student's  $t$ -test), empty circles indicate non-significant differences. NH: Northern Hemisphere; SH: Southern Hemisphere. [Colour figure can be viewed at [wileyonlinelibrary.com](http://wileyonlinelibrary.com)]

(a) 50 hPa ( $\text{m}\cdot\text{s}^{-1}$ )(b) 300 hPa ( $\text{m}\cdot\text{s}^{-1}$ )

(c) 500 hPa (gpm)

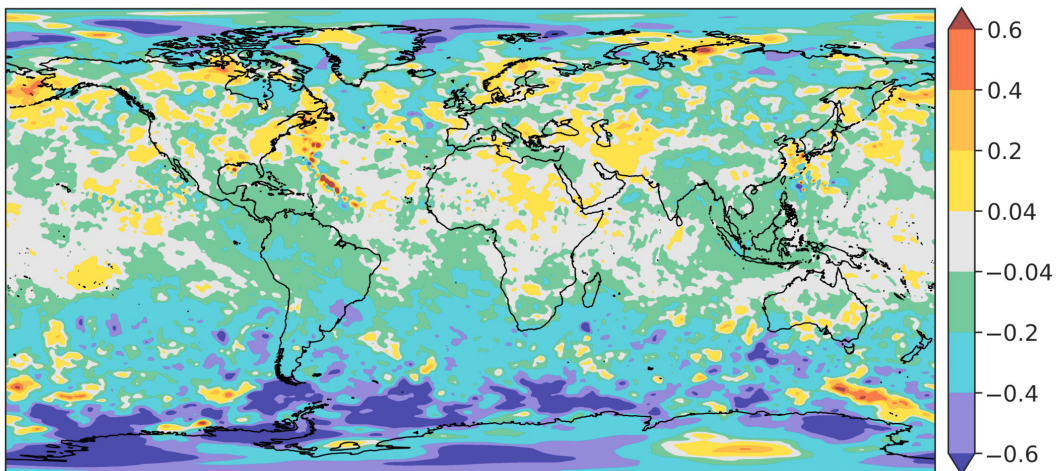


**FIGURE 7** The mean differences in 24- to 96-hr forecast root-mean-squared error between the EXP\_A and the CTRL run as function of pressure (hPa) for July 1, 2020, to September 30, 2020: (a) 50 hPa zonal wind component  $U$ , (b) 300 hPa zonal wind component  $U$ , and (c) 500 hPa geopotential  $Z$ . [Colour figure can be viewed at [wileyonlinelibrary.com](http://wileyonlinelibrary.com)]

the stratosphere. Presumably, the impact on RH is mainly caused by improved winds leading to improved advection of humidity and a resulting relative reduction in the humidity RMSE up to 2%. In the midlatitudinal troposphere of the Southern Hemisphere, the RMSE is reduced up to 3% for the zonal wind and temperature and even up to 6% for geopotential. In the midlatitudes of the Northern Hemisphere, Aeolus observations lead to an average improvement of up to 1%, which is again consistent with the changes in forecast errors verified against wind and temperature observations from radiosondes, aircraft, and AMVs (Section 4.2). Towards the polar regions, the differences in impact between forecast lead times shorter and longer than 3 days become larger. Especially in the Southern Hemisphere, differences in the sign of the impact occur with increased degradation in forecast quality for the 96 and 120 hr forecasts. This may be due to the generally larger model errors in the polar regions, especially in the Southern Hemisphere, and the strong systematic differences between ERA5 based on the IFS model and the ICON experiments in these regions (Figure 3). However, statistically significant effects in the polar regions arise mainly for shorter forecast lead times.

Figure 7 provides an overview of the spatial distribution of the impact. The mean changes in the analysis field of zonal wind due to Aeolus HLOS winds and the global impact statistics showed a particularly pronounced structural influence in the upper atmospheric levels of the Tropics. Figure 7a,b displays the spatial distribution of RMSE reduction of the 24- to 96-hr zonal wind forecast for the stratospheric and tropospheric jet levels, indicating that the beneficial impact is mainly located around the equatorial band at 50 hPa that is affected by the QBO pattern and around the eastern Pacific at 300 hPa, where the interaction between surface temperatures and upper level winds (ENSO) dominates the large-scale dynamics. Thus, the strong influence on the analysis in the lower stratosphere shown in Figures 3a and 4 is associated with overall improvements in the forecast. Large uncertainties in the analysis and a pronounced influence of the Aeolus observations had also previously been shown in the eastern Pacific region around the tropospheric jet levels (Figure 3c,d). As the OSE period covers the changes in the circulation state of these two atmospheric phenomena, we assume that the large error reduction is related to errors in the phase change of these circulation systems.

Besides the Tropics and the poorly observed Southern Hemisphere, the relative impact statistics showed a significant impact of assimilating Aeolus winds for the short-range forecast lead times in the Northern Hemisphere. The medium-range impact pattern demonstrated in Figure 7c for the 500 hPa geopotential shows a lot of variability in the Northern Hemisphere. In particular,

there are fluctuations in the flow regime of storm track regions (e.g., the North Atlantic and West Pacific), which are likely to obscure the mean error reduction. During the development of the Aeolus mission, several scientific and campaign activities found that DWL wind observations benefit the poorly predicted severe storm events (Marseille *et al.*, 2008a), such as tropical cyclones and their interaction with the midlatitude dynamics (Pu *et al.*, 2010; Weissmann *et al.*, 2012). Further investigation of these effects and dynamical interpretation of the spatial and temporal evolution of the forecast error reduction can be found in Martin *et al.* (2023).

In addition to the midlatitudes, a large impact is also visible in the polar regions. To some extent, this is assumed to be related to the dense observational coverage due to the smaller distance between the Aeolus orbit around the poles. In the Northern Hemisphere, the weaker and often meandering polar vortex in the summer months could be better represented by assimilating the Aeolus observations. Moreover, both the high latitudes in the Northern and Southern Hemispheres show some dipole structure, which was also found in the Aeolus influence on the analysis (Figure 3). So far, however, it is not clear which dynamical processes lead to the large influence and spatial distribution. Future reprocessed datasets that provide longer term consistent Aeolus wind data will enable OSEs over a longer period of time, which would significantly contribute to a better understanding of the Aeolus impact in global NWP.

## 5 | CONCLUSIONS

The Aeolus HLOS wind observations derived from Rayleigh and Mie scattering on a global scale are expected to make a valuable contribution to the GOS, filling the gap of insufficient coverage of wind profiles, especially over oceans, the Tropics, and the Southern Hemisphere. This study aims to assess the usefulness of the Aeolus data and future space-based DWL observations in the global model ICON from DWD by providing a global statistical overview of the systematic changes in the analysis and the impact on forecast errors. Therefore, a 3-month OSE from July 2020 to October 2020 has been conducted using the operational setting of the global assimilation system of ICON with a horizontal resolution of 13 km.

Observation minus background and random error statistics have served to evaluate the data quality for the selected experiment period and its consistency with error assumptions used in the data assimilation system (Section 3). An investigation of the systematic errors has revealed a height dependency for the Rayleigh winds, which could be successfully reduced by a model-based bias correction as a function of latitude for specific height

levels, separately for ascending and descending orbits. The vertical structure of the standard deviation of the  $O - B$  departures, the observation error provided by the L2B processor, and the observation error assigned in the assimilation have been found to agree relatively well, indicating a consistent slightly higher precision of Aeolus observations in the midtroposphere compared with upper levels. The assigned observation error was found to be a good proxy for the measurement error estimate of the Rayleigh winds, whereas the Mie observations have appeared to be somewhat underweighted in the assimilation system. As the Rayleigh wind random errors depend on vertical sampling, the adjustment of the range-bin setting in 2020 has resulted in increased uncertainties in the levels around the jet stream. Overall, the Aeolus HLOS winds have shown small but somewhat complex systematic differences, as well as random error estimates that are larger than expected at the start of the mission. However, the error components are still fairly consistent and stable for the OSE period. Since the Aeolus observations are a novel data type and technical problems can constantly affect their quality, the evaluation and monitoring as performed in Section 3 is a prerequisite for the assimilation.

The effect of assimilating Aeolus HLOS winds in ICON has been assessed through the investigation of systematic changes in the analysis (Section 4.1), changes in the short-range forecast quality when verified against conventional observation types (Section 4.2), and changes in forecast quality up to 120 hr using ERA5 as verification data (Section 4.3). The systematic analysis influence of the Aeolus observations has been found to be most pronounced in jet regimes, around large-scale circulation systems and convectively active areas in the Tropics, where the analysis uncertainties are systematically larger, and the coverage of other observations is poor. In particular, the equatorial stratosphere and the upper troposphere in the East Pacific have shown increased systematic changes in the zonal wind analysis.

The impact of the Aeolus HLOS winds verified against observations from radiosondes, aircraft, GNSS-ROs, and AMVs for short-range forecasts up to 36 hr overall is found to be clearly beneficial, particularly in the Tropics and the Southern Hemisphere if the sample size of  $O - B$  values is large enough (on average 0.5–1.6% RMSE reduction). In the Northern Hemisphere, an RMSE reduction of 0.1–0.6% is achieved. Impact statistics for forecast lead times from 24 to 120 hr have shown the largest improvements in the Tropics. The error of zonal wind forecasts around the tropical tropopause height is significantly reduced by up to 8% when Aeolus winds are assimilated. In the Southern Hemisphere, a positive impact has predominantly appeared below the tropopause, with the largest improvements of 6% in geopotential and 5% in temperature and

zonal wind. The impact in the Northern Hemisphere is smaller and only significant for short-range lead times, with a maximum of 3% in the midtroposphere. Unlike the midlatitudes and Tropics, the polar regions exhibit some differences in impact between forecast lead times shorter or longer than 3 days. This is likely related to larger systematic differences between ERA5 based on the IFS model and the ICON experiments above 60°.

Our study investigates the impact of Aeolus over a 3-month period, and it should be noted that results may differ in different seasons and depending on the quality of the Aeolus data, which have changed over time due to changes in instrument performance and also data processing. Future studies will be able to conduct longer experiments with consistently processed data that will allow one to examine effects such as the seasonal dependence of the Aeolus impact. Compared with already published studies about the Aeolus impact studies in the ECMWF, Météo-France, NOAA, and ECCO global forecast system, the improvements in the global model ICON of DWD is comparably large with up to 4% error reduction. These impact studies all used L2B HLOS wind data based on baseline 2B10, but they differ in data assimilation algorithm, model resolution of the OSE, assigned observation error, model-based bias correction, and the set of the other assimilated observations. One major difference of our OSE compared with the other studies is the 3DVar assimilation system at DWD. Owing to the missing time component, the system can extract less wind information from satellite radiances. Furthermore, for example, at ECMWF, about 98% of operational assimilated observations are provided by satellite systems, which is about 15 times more than at DWD. Therefore, at ECMWF, a single spaceborne lidar instrument has a smaller impact on the analysis and forecasts. Also, the up to two times higher horizontal resolution of the OSE investigated in this study compared with other impact evaluations probably leads to the larger impact. However, an additional detailed examination would be necessary to evaluate the contribution of the specific differences of the Aeolus impact studies.

Regions of particularly large forecast error reduction in the OSE period are found in the equatorial band in the lower stratosphere and around the eastern Pacific at the tropospheric jet levels, indicating the large systematic changes in the analysis there are, on average, improvements. The overall beneficial impact in the Northern Hemisphere is likely obscured by large variability in spatial distribution and does not appear systematic at first. A better understanding of the underlying dynamics leading to the large mean Aeolus observation impact requires investigations of the spatiotemporal development of the forecast error reductions. Therefore, the present study can be considered a prelude to a more comprehensive study

focusing on the forecast quality of specific high-impact events (Martin *et al.*, 2023).

## AUTHOR CONTRIBUTIONS

**Anne Martin:** investigation; visualization; writing – original draft. **Martin Weissmann:** conceptualization; methodology; supervision; writing – review and editing. **Alexander Cress:** data curation; resources; writing – review and editing.

## ACKNOWLEDGEMENTS

This work was funded by the German Federal Ministry for Economic Affairs and Climate Action (BMWK) under grant number (FKZ) 50EE1721A and further supported by the Transregional Collaborative Research Center Waves to Weather (W2W) (SFB/TRR165) funded by the German Research Foundation (DFG). We thank the ESA for providing the Aeolus datasets. In addition, we are very grateful to the EVAA consortium (LMU, DWD, DLR) and the Aeolus Cal/Val community, who made helpful contributions to this work in many valuable discussions. Open Access funding enabled and organized by Projekt DEAL.

## CONFLICT OF INTEREST STATEMENT

The authors affirm that they have no conflict of interest.

## ORCID

Anne Martin  <https://orcid.org/0000-0002-8712-5329>

## REFERENCES

- Anstey, J.A., Banyard, T.P., Butchart, N., Coy, L., Newman, P.A., Osprey, S. and Wright, C.J. (2021) Prospect of increased disruption to the QBO in a changing climate. *Geophysical Research Letters*, 48, e2021GL093058. <https://doi.org/10.1029/2021GL093058>.
- Baars, H., Herzog, A., Heese, B., Ohneiser, K., Hanbuch, K., Hofer, J., Yin, Z., Engelmann, R. and Wandinger, U. (2020) Validation of Aeolus wind products above the Atlantic Ocean. *Atmospheric Measurement Techniques*, 13, 6007–6024. <https://doi.org/10.5194/amt-13-6007-2020>.
- Baker, W.E., Atlas, R., Cardinali, C., Clement, A., Emmitt, G.D., Gentry, B.M., Hardesty, R.M., Källén, E., Kavaya, M.J., Langleland, R., Ma, Z., Masutani, M., McCarty, W., Pierce, R.B., Pu, Z., Riishojgaard, L.P., Ryan, J., Tucker, S., Weissmann, M. and Yoe, J. (2014) Lidar-measured wind profiles: the missing link in the global observing system. *Bulletin of the American Meteorological Society*, 95, 543–564. <https://doi.org/10.1175/BAMS-D-12-00164.1>.
- Belova, E., Kirkwood, S., Voelger, P., Chatterjee, S., Satheesan, K., Hagelin, S., Lindskog, M. and Körnich, H. (2021) Validation of Aeolus winds using ground-based radars in Antarctica and in northern Sweden. *Atmospheric Measurement Techniques*, 14, 5415–5428. <https://doi.org/10.5194/amt-14-5415-2021>.
- Bormann, N., Saarinen, S., Kelly, G. and Thépaut, J.-N. (2003) The spatial structure of observation errors in atmospheric motion vectors from geostationary satellite data. *Quarterly Journal of the Royal Meteorological Society*, 131, 706–718. [https://doi.org/10.1175/1520-0493\(2003\)131<0706:TSSOOE>2.0.CO;2](https://doi.org/10.1175/1520-0493(2003)131<0706:TSSOOE>2.0.CO;2).
- Borne, M., Knippertz, P., Weissmann, M., Martin, A., Rennie, M. and Cress, A. (2022) Impact of Aeolus wind lidar observations on the representation of the west African monsoon circulation in the ECMWF and DWD modeling systems.
- Dabas, A., Denneulin, M., Flamant, P., Loth, C., Garnier, A. and Dolfi-Bouteyre, A. (2008) Correcting winds measured with a Rayleigh Doppler lidar from pressure and temperature effects. *Tellus*, 60 A, 206–215. <https://doi.org/10.1111/j.1600-0870.2007.00284.x>.
- Desroziers, G., Berre, L., Chapnik, B. and Poli, P. (2005) Diagnosis of observation, background and analysis-error statistics in observation space. *Quarterly Journal of the Royal Meteorological Society*, 131, 3385–3396. <https://doi.org/10.1256/qj.05.108>.
- ECMWF. (2023) Aeolus HLOS wind observation monitoring. <https://charts.ecmwf.int/catalogue/packages/obstat/?facets=%7B%22Data%20type%22%3A%5B%22Aeolus%20HLOS%20Wind%22%5D%7D>.
- ESA. (2008) ADM-Aeolus Science Report. ESA SP-1311, 121. <https://earth.esa.int/documents/10174/1590943/AEOL002.pdf>.
- ESA. (2016) ADM-Aeolus Mission requirements documents. ESA EOP-SM/2047, 57. [http://esamultimedia.esa.int/docs/EarthObservation/ADM-Aeolus\\_MRD.pdf](http://esamultimedia.esa.int/docs/EarthObservation/ADM-Aeolus_MRD.pdf).
- Folger, K. and Weissmann, M. (2014) Height correction of atmospheric motion vectors using satellite lidar observations from CALIPSO. *Journal of Applied Meteorology and Climatology*, 53, 1809–1819. <https://doi.org/10.1175/JAMC-D-13-0337.1>.
- Garrett, K., Liu, H., Ide, K., Hoffman, R.N. and Lukens, K.E. (2022) Optimization and impact assessment of Aeolus HLOS wind assimilation in NOAA's global forecast system. *Quarterly Journal of the Royal Meteorological Society*, 148, 2703–2716.
- Geer, A.J., Bauer, P. and Lopez, P. (2010) Direct 4D-Var assimilation of all-sky radiances. Part II: assessment. *Quarterly Journal of the Royal Meteorological Society*, 136, 1886–1905. <https://doi.org/10.1002/qj.681>.
- Geiß, A., Lehmann, V., Leinweber, R., Reitebuch, O. and Weissmann, M. (2020) Validation of the Aeolus L2B product with operational radar wind profiler measurements. Aeolus Cal/Val and Science Workshop 2020. <https://nikal.eventsair.com/QuickEventWebsitePortal/2nd-aeolus-post-launch-calval-and-science-workshop/aeolus>.
- Goody, R.M. and Walker, J.C.G. (1972) *Atmospheres*. Englewood Cliffs, NJ: Prentice-Hall.
- Horányi, A., Cardinali, C., Rennie, M. and Isaksen, L. (2015a) The assimilation of horizontal line-of-sight wind information into the ECMWF data assimilation and forecasting system. Part I: the assessment of wind impact. *Quarterly Journal of the Royal Meteorological Society*, 141, 1223–1232. <https://doi.org/10.1002/qj.2430>.
- Horányi, A., Cardinali, C., Rennie, M. and Isaksen, L. (2015b) The assimilation of horizontal line-of-sight wind information into the ECMWF data assimilation and forecasting system. Part II: the impact of degraded wind observations. *Quarterly Journal of the Royal Meteorological Society*, 141, 1233–1243. <https://doi.org/10.1002/qj.2551>.
- Khaykin, S.M., Hauchecorne, A., Wing, R., Keckhut, P., Godin-Beekmann, S., Porteneuve, J., Mariscal, J.-F. and Schmitt, J. (2020) Doppler lidar at Observatoire de haute-Provence for

- wind profiling up to 75 km altitude: performance evaluation and observations. *Atmospheric Measurement Techniques*, 13, 1501–1516. <https://doi.org/10.5194/amt-13-1501-2020>.
- Laroche, S. and St-James, J. (2022) Impact of the Aeolus level-2B horizontal line-of-sight winds in the environment and climate change Canada global forecast system. *Quarterly Journal of the Royal Meteorological Society*, 148, 2047–2062. <https://doi.org/10.1002/qj.4300>.
- Liu, B., Guo, J., Gong, W., Zhang, Y., Shi, L., Ma, Y., Li, J., Guo, X., Stoffelen, A., de Leeuw, G. and Xu, X. (2022) Intercomparison of wind observations from ESA's satellite mission Aeolus, ERA5 reanalysis and radiosonde over China. *Atmospheric Measurement Techniques Discussions*, 2022, 1–32. <https://doi.org/10.5194/amt-2022-26>.
- Lux, O., Lemmerz, C., Weiler, F., Marksteiner, U., Witschas, B., Rahm, S., Geiß, A. and Reitebuch, O. (2020) Intercomparison of wind observations from the European Space Agency's Aeolus satellite mission and the ALADIN airborne demonstrator. *Atmospheric Measurement Techniques*, 13, 2075–2097. <https://doi.org/10.5194/amt-13-2075-2020>.
- Marseille, G., Stoffelen, A. and Barkmeijer, J. (2008a) A cycled sensitivity observing system experiment on simulated Doppler wind lidar data during the 1999 Christmas storm 'Martin'. *Tellus A: Dynamic Meteorology and Oceanography*, 60A, 249–260. <https://doi.org/10.1111/j.1600-0870.2007.00290.x>.
- Marseille, G.J., de Kloe, J., Marksteiner, U., Reitebuch, O., Rennie, M. and de Haan, S. (2022) NWP calibration applied to Aeolus Mie channel winds. *Quarterly Journal of the Royal Meteorological Society*, 148, 1020–1034. <https://doi.org/10.1002/qj.4244>.
- Marseille, G.-J., Stoffelen, A. and Barkmeijer, J. (2008b) Impact assessment of prospective spaceborne Doppler wind lidar observation scenarios. *Tellus*, 60A, 234–248. <https://doi.org/10.1111/j.1600-0870.2007.00289.x>.
- Martin, A., Weissmann, M. and Cress, A. (2023) Investigation of links between dynamical scenarios and particularly high impact of aeolus on numerical weather prediction (nwp) forecasts. *Weather and Climate Dynamics*, 4, 249–264 <https://wcd.copernicus.org/articles/4/249/2023/>.
- Martin, A., Weissmann, M., Reitebuch, O., Rennie, M., Geiß, A. and Cress, A. (2021) Validation of Aeolus winds using radiosonde observations and numerical weather prediction model equivalents. *Atmospheric Measurement Techniques*, 14, 2167–2183. <https://doi.org/10.5194/amt-14-2167-2021>.
- Pourret, V., Šavli, M., Mahfouf, J.-F., Raspaud, D., Doerenbecher, A., Bénichou, H. and Payan, C. (2022) Operational assimilation of Aeolus winds in the Météo-France global NWP model ARPEGE. *Quarterly Journal of the Royal Meteorological Society*, 148(747), 2652–2671. <https://doi.org/10.1002/qj.4329>.
- Pu, Z., Zhang, L. and Emmitt, G.D. (2010) Impact of airborne Doppler wind lidar profiles on numerical simulations of a tropical cyclone. *Geophysical Research Letters*, 37, L05801. <https://doi.org/10.1029/2009GL041765>.
- Reinert, D., Prill, F., Frank, H., Denhard, M., Baldauf, M., Schraff, C., Gebhardt, C., Marsigli, C. and Zängl, G. (2023) DWD database reference for the global and regional ICON and ICON-EPS forecasting system. [https://www.dwd.de/DWD/forschung/nwv/fepub/icon\\_database\\_main.pdf](https://www.dwd.de/DWD/forschung/nwv/fepub/icon_database_main.pdf).
- Reitebuch, O. (2012) The Spaceborne wind Lidar Mission ADM-Aeolus. In U. Schumann (Ed.), *Atmospheric Physics: Background-Methods-Trends*, (pp. 815–827). Berlin Heidelberg: Springer Berlin Heidelberg.
- Reitebuch, O., Lemmerz, C., Lux, O., Marksteiner, U., Rahm, S., Weiler, F., Witschas, B., Meringer, M., Schmidt, K., Huber, D., Nikolaus, I., Geiß, A., Vaughan, M., Dabas, A., Flament, T., Stieglitz, H., Isaksen, L., Rennie, M., de Kloe, J., Marseille, G.J., Stoffelen, A., Wernham, D., Kanitz, T., Straume, A.G., Fehr, T., von Bismarck, J., Floberghagen, R. and Parrinello, T. (2020) Initial assessment of the performance of the first wind Lidar in space on Aeolus. *EPJ Web Conference*, 237, 01010. <https://doi.org/10.1051/epjconf/202023701010>.
- Rennie, M. and Isaksen, L. (2020) The NWP impact of Aeolus level-2B winds at ECMWF. *Technical Memorandum ECMWF*, 864 <https://www.ecmwf.int/node/19538>.
- Rennie, M., Isaksen, L., Weiler, F., de Kloe, J., Kanitz, T. and Reitebuch, R. (2021) The impact of Aeolus wind retrievals on ECMWF global weather forecast. *Quarterly Journal of the Royal Meteorological Society*, 1–32, 3555–3586. <https://doi.org/10.1002/qj.4142>.
- Rennie, M., Tan, D.G.H., Andersson, E., Poli, P., Dabas, A., de Kloe, J., Marseille, G.-J. and Stoffelen, A. (2020) Aeolus level-2B algorithm theoretical basis document (mathematical description of the Aeolus level-2B processor). AE-TN-ECMWF-L2BP.0023, 3.21.
- Rhodin, A. (2015) *Multi Scale VarEnKF Localisation Using Wavelets*. RIKEN: Presentation at International Symposium on Data Assimilation. <http://www.data-assimilation.riken.jp/isda2015/program/pdf/8-4.pdf>.
- Šavli, M., Pourret, V., Payan, C. and Mahfouf, J.-F. (2021) Sensitivity of Aeolus HLOS winds to temperature and pressure specification in the L2B processor. *Atmospheric Measurement Techniques*, 14, 4721–4736. <https://doi.org/10.5194/amt-14-4721-2021>.
- Stoffelen, A., Marseille, G.-J., Bouttier, F., Vasiljevic, D., de Haan, S. and Cardinali, C. (2006) ADM-Aeolus Doppler wind lidar observing system simulation experiment. *Quarterly Journal of the Royal Meteorological Society*, 132, 1927–1947. <https://doi.org/10.1256/qj.05.83>.
- Tan, D.G.H. and Andersson, E. (2005) Simulation of the yield and accuracy of wind profile measurements from the atmospheric dynamics Mission (ADM-Aeolus). *Quarterly Journal of the Royal Meteorological Society*, 131, 1737–1757. <https://doi.org/10.1256/qj.04.02>.
- Tan, D.G.H., Andersson, E., Fisher, M. and Isaksen, L. (2007) Observing-system impact assessment using a data assimilation-ensemble technique: application to the ADM Aeolus wind profiling mission. *Quarterly Journal of the Royal Meteorological Society*, 133, 381–390. <https://doi.org/10.1002/qj.43>.
- Tan, D.G.H., Andersson, E., Kloe, J.D., Marseille, G.-J., Stoffelen, A., Poli, P., Denneulin, M.-L., Dabas, A., Huber, D., Reitebuch, O., Flamant, P., Rille, O.L. and Nett, H. (2008) The ADM-Aeolus wind retrieval algorithms. *Tellus A: Dynamic Meteorology and Oceanography*, 60, 191–205. <https://doi.org/10.1111/j.1600-0870.2007.00285.x>.
- Weiler, F., Rennie, M., Kanitz, T., Isaksen, L., Checa, E., de Kloe, J., Okunde, N. and Reitebuch, O. (2021) Correction of wind bias for the lidar on board Aeolus using telescope temperatures. *Atmospheric Measurement Techniques*, 14, 7167–7185. <https://doi.org/10.5194/amt-14-7167-2021>.
- Weissmann, M. and Cardinali, C. (2007) Impact of airborne Doppler lidar observations on ECMWF forecasts. *Quarterly Journal of the*

- Royal Meteorological Society*, 133, 107–116. <https://doi.org/10.1002/qj.16>.
- Weissmann, M., Langland, R.H., Cardinali, C., Pauley, P.M. and Rahm, S. (2012) Influence of airborne Doppler wind lidar profiles near typhoon Sinlaku on ECMWF and NOGAPS forecasts. *Quarterly Journal of the Royal Meteorological Society*, 138, 118–130. <https://doi.org/10.1002/qj.896>.
- Witschas, B., Lemmerz, C., Geiß, A., Lux, O., Marksteiner, U., Rahm, S., Reitebuch, O. and Weiler, F. (2020) First validation of Aeolus wind observations by airborne Doppler wind lidar measurements. *Atmospheric Measurement Techniques*, 13, 2381–2396. <https://doi.org/10.5194/amt-13-2381-2020>.
- WMO. (1996) Guide to meteorological instruments and methods of observation-6th edition. WMO-No. 8, 681.
- Žagar, N. (2004) Assimilation of equatorial waves by line of sight wind observations. *Journal of Atmospheric Science*, 61, 1877–1893. [https://doi.org/10.1175/1520-0469\(2004\)061<1877:AOEWBL>2.0.CO;2](https://doi.org/10.1175/1520-0469(2004)061<1877:AOEWBL>2.0.CO;2).
- Zängl, G., Reinert, D., Ripodas, P. and Baldauf, M. (2015) The ICON (ICOsahedral non-hydrostatic) modelling framework of DWD and MPI-M: description of the non-hydrostatic dynamical core. *Quarterly Journal of the Royal Meteorological Society*, 141, 563–579. <https://doi.org/10.1002/qj.2378>.
- Zhang, L. and Pu, Z. (2010) An observing system simulation experiment (OSSE) to assess the impact of Doppler wind Lidar (DWL) measurements on the numerical simulation of a tropical cyclone. *Advances in Meteorology*, 2010, 1687–9309. <https://doi.org/10.1155/2010/743863>.

**How to cite this article:** Martin, A., Weissmann, M. & Cress, A. (2023) Impact of assimilating Aeolus observations in the global model ICON: A global statistical overview. *Quarterly Journal of the Royal Meteorological Society*, 149(756), 2962–2979. Available from: <https://doi.org/10.1002/qj.4541>